

Revealing Actual Viscoelastic Relaxation Times in Capillary Breakup

Nan Hu,^{1,*} Jonghyun Hwang,¹ Tachin Ruangkriengsin,² and Howard A. Stone^{1,†}

¹*Department of Mechanical and Aerospace Engineering, Princeton University, NJ 08544, USA*

²*Program in Applied and Computational Mathematics, Princeton University, NJ 08544, USA*

(Dated: March 25, 2025)

We use experiments and theory to elucidate the size effect in capillary breakup rheometry, where pre-stretching in the visco-capillary stage causes the apparent relaxation time to be consistently smaller than the actual value. We propose a method accounting for both the experimental size and the finite extensibility of polymers to extract the actual relaxation time. A phase diagram characterizes the expected measurement variability and delineates scaling law conditions. The results refine capillary breakup rheometry for viscoelastic fluids and advance the understanding of breakup dynamics across scales.

Capillary thinning and breakup of viscoelastic liquid threads are ubiquitous in natural environments, biological tissues, and industrial applications [1–3]. Unlike viscous liquids, the capillary breakup of viscoelastic liquids exhibits distinct behaviors such as the exponential decay of filament thinning [4–7] and the formation of satellite droplets on a string [8–11], which are attributed to the elastic forces from polymeric stresses. Consequently, capillary breakup rheometry, which leverages these dynamic characteristics, has been a method widely used to measure viscoelastic properties, and is especially promising for weakly-elastic fluids [12] and biopolymers such as DNA [13, 14], whose properties are difficult to measure using common rheometric methods. Current well-developed experimental techniques include stretching a liquid bridge between two plates (known as CaBER) [15–18], jetting [19–22], dripping [23, 24], and dripping-onto-substrate (DoS) [25–28].

Typically, the capillary breakup of viscoelastic fluids is governed by the interplay of inertial, viscous, elastic, and surface tension forces. Based on the sequence of events during the breakup of droplets or liquid bridges, the dynamics can be categorized into the visco-capillary (VC) or inertial-capillary (IC) stage, the elasto-capillary (EC) stage, and the final visco-elasto-capillary (VEC) stage [29]. By assuming infinite extensibility of the polymer chains ($b = \infty$) with a (longest) relaxation time λ , the evolution of the neck diameter $D(t)$ for the EC stage is well-known as

$$D(t)/D_1 = (GD_1/2\gamma)^{1/3} \exp[-(t - t_1)/3\lambda], \quad (1)$$

where G is the modulus of the viscoelastic fluid, D_1 is the initial diameter of the liquid filament, γ is the surface tension, and t_1 is the time of onset of the EC stage [4]. This formula has been adopted in numerous studies to interpret the experimental results of the variation of the filament diameter $D(t)$ during the EC stage. Thus, one obtains an estimate of the apparent relaxation time λ_e for various kinds of polymer solutions by fitting the exponential decay [12, 15, 25–27, 29–33].

However, existing studies have found that pre-stretching of the polymers or filament thinning during

the IC/VC stage significantly influences the exponential decay in the subsequent EC stage [14, 17, 18, 23, 32]. The sensitivity of λ_e to these effects can be attributed to several experimental parameters, including the initial separation rate of the plates [17], the initial diameter D_0 of the liquid bridge [18] in the CaBER method, nozzle diameter ℓ in the dripping method (where $\lambda_e \propto \ell^{8/9}$ has been observed) [23], and the polymer extensibility parameter b in the DoS method [32]. This parameter dependence introduces strong sensitivity of the extracted relaxation time λ_e to initial conditions and inevitable pre-stretching effects in capillary breakup rheometry. While several studies have reported such dependence [18, 23, 32], no work has yet directly identified the actual relaxation time λ from breakup measurements, nor established a general scaling law relating λ_e to ℓ or D_0 . In contrast, a recent study [33] reported no systematic dependence of λ_e on CaBER plate size across four polymer solutions with varying concentration and molecular weight. This highlights the need for a unified framework to account for the size-dependent variability of λ_e observed in different experimental systems.

In this Letter we demonstrate that size-dependent apparent relaxation times, λ_e , obtained from capillary breakup processes of varying scales, can be used to estimate the actual relaxation time, λ , while simultaneously determining the extensibility, b , representative of the polymer solution. In particular, accounting for finite extensibility b , we show that pre-stretching during the VC stage shortens the exponential decay in the elasto-capillary stage, leading to $\lambda_e < \lambda$, and that this effect can be dependent on the size of the experimental setups. Through experiments and numerical solutions, we unravel this quantitative relationship, enabling the determination of the actual relaxation time λ from both our measurements and those reported in recent studies.

The capillary breakup processes considered here include dripping, DoS, and CaBER (Fig. 1a (i, ii, iii)). In all cases, the liquid initially is slowly stretched in a quasi-static manner within devices of characteristic size ℓ . Under the action of capillary forces driving the Rayleigh-Plateau instability, the liquid rapidly contracts from the

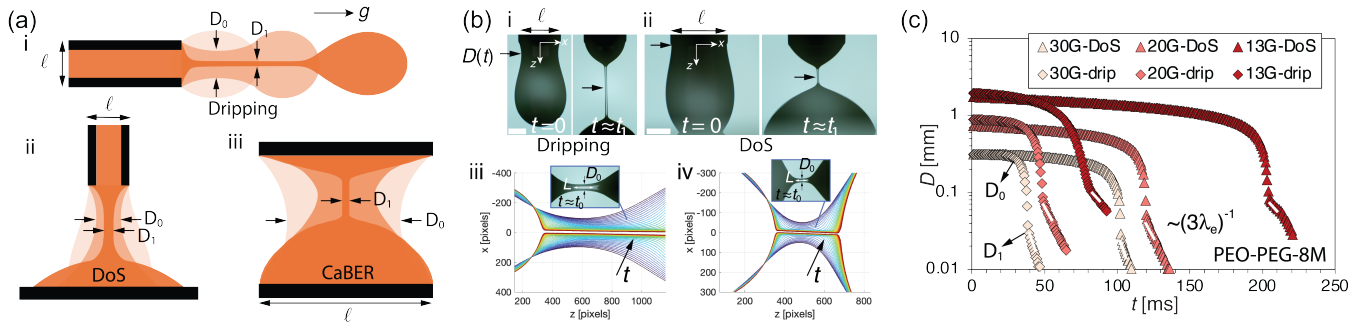


FIG. 1. Capillary breakup rheometry. (a) Schematic illustrations of liquid filament breakup for different experimental configurations: (i) dripping, (ii) dripping-onto-substrate (DoS), and (iii) a liquid bridge between two plates (classic CaBER). The liquid is initially held quasi-steady by a nozzle or plates with diameter ℓ . The minimum neck diameter of the liquid, $D(t)$, evolves over time from the D_0 to D_1 , where subscripts 0 and 1 mark the onset of the VC and EC stages, respectively. (b) Representative measurements for a PEO-PEG-8M solution using (i) dripping and (ii) DoS methods with a 13G nozzle ($\ell = 2.4$ mm). (iii) and (iv) are the extracted evolutions of interface shapes with increasing time t corresponding, respectively, to dripping and DoS, where D_0 is estimated by taking the filament aspect ratio $1 \lesssim L/D_0 \lesssim 3$. Scale bars represent 1 mm. (c) Representative datasets showing the variation of $D(t)$ for different $\ell \in \{0.3, 0.9, 2.4\}$ mm and methods (different symbols). Distinct slopes of $\log_{10} D$ in the EC stage for varying ℓ indicate a size-dependent apparent relaxation time λ_e predicted by the slope $\sim (3\lambda_e)^{-1}$.

initial diameter D_0 of the VC stage to the initial diameter D_1 of the EC stage. In our experiments, we used needles with varying outer diameter $\ell \in \{0.3, 0.5, 0.9, 1.8, 2.4\}$ mm (corresponding to 30G, 25G, 20G, 15G, and 13G needles) to conduct tests using the dripping and DoS methods. Given that the influence of the size of the CaBER method has been tested in Ref. [18, 33], we also used their data of the PEOvis and PS solution (see [34], §I and Fig. S1) for our analysis.

Three kinds of polymer solutions were employed in our experiments: PIB-PB (polyisobutylene dissolved in a polybutene-mineral oil mixed solvent), PS-DOP (polystyrene dissolved in the organic solvent dioctyl phthalate), and PEO-PEG (polyethylene oxide dissolved in a polyethylene glycol-water solution), whereas PIB-PB-0.3 and PIB-PB-0.02 denote different PIB concentrations; PEO-PEG-8M and PEO-PEG-1M identify different molecular weights of PEO. These latter fluids can be regarded as Boger fluids with constant viscosity (Fig. S2 [34]), ensuring that additional effects from viscosity variations with extension rate are eliminated. Detailed preparation procedures and physical property measurements, such as viscosity η_0 , surface tension γ , storage modulus G' , and loss modulus G'' , are provided in [34] §II and summarized in Table S1. The polymer concentrations c used in this study fall within the dilute regime, with $c^* > c \gtrsim 0.1c^*$, and are all significantly higher than the minimal concentrations required for EC stage [35, 36]. These include $c_{\min} \sim c^*/b$ and $c_{\text{low}} \sim c^*/b^{0.75}$, which represent the thresholds for the emergence of the EC regime [35] and for visibly observable exponential thinning [36], respectively.

Capillary breakup tests were conducted inside a transparent chamber to shield the system from air disturbances, with a liquid reservoir included to minimize the

effects of evaporation (see [34] §III). High-speed imaging was conducted using a camera (VEO 640L, Phantom) equipped with microscope objectives (Nikon) of 2X, 5X, or 10X magnifications to accommodate varying nozzle diameters. A syringe pump (PHD 2000, Harvard Apparatus) controlled the flow rate at $Q = 1 - 10 \mu\text{L}/\text{min}$, ensuring a quasi-static droplet for dripping. Taking the PEO-PEG-8M solution as an example, representative snapshots from the dripping and DoS tests, captured at a resolution of 2560×1600 pixels and 1500 frames per second (fps), are shown in Fig. 1(b-i, ii), respectively. The liquid surface was analyzed using a custom MATLAB image-processing algorithm to track the gas-liquid interface as depicted in Fig. 1(b-iii, iv), in order to obtain the evolution of the minimum neck diameter $D(t)$ (Fig. 1c). Unlike the CaBER method, where the instability can be triggered in a controlled manner by adjusting the plate spacing to directly determine D_0 , we propose that in the dripping and DoS methods, D_0 should be determined by ensuring $1 \lesssim L/D_0 \lesssim 3$ (Fig. 1b-iii, iv, detailed discussion seen in [34] §V). Each case was repeated at least three times to confirm data reproducibility. The results for the other solutions are provided in Fig. S4 [34].

The transition in the $D(t)$ curves and the appearance of a uniform filament (Fig. 1b-i, ii) allow the determination of the initial diameter D_1 for the EC stage. Using Eq. (1), a fit following this point (white lines in Fig. 1c) yields the value of λ_e . The results show that λ_e increases with the nozzle diameter ℓ , though no significant difference is observed between the λ_e values obtained from the dripping and DoS methods. We conducted a comprehensive comparison of the apparent relaxation times λ_e for different viscoelastic fluids, nozzle diameters ℓ , and testing methods (Fig. 2). We observed that PEO-PEG, PIB-PB-0.02, and PEOvis solutions exhibit a size dependence

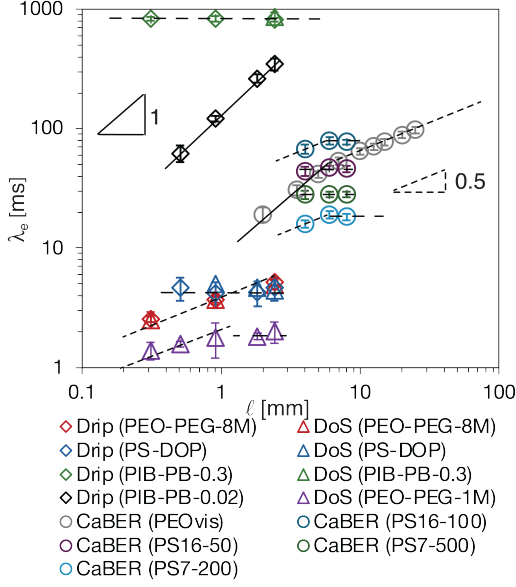


FIG. 2. Dependence of apparent relaxation time λ_e on apparatus size ℓ for different Boger fluids using specific methods: PEO-PEG, PS-DOP, PIB-PB in this work by dripping and/or DoS, PEOvis (Ref. [18]) and PS16/PS7 (Ref. [33]) by CaBER.

of λ_e , showing a variation from $\sim \ell$ to $\sim \ell^{0.5}$ with increasing ℓ for one fluid. In contrast, λ_e values of the PS-DOP and PIB-PB-0.3 solution remain nearly constant.

We believe that viscoelastic fluids formed from nearly monodisperse polymer solutions should exhibit a constant intrinsic (longest) relaxation time λ , independent of testing conditions; indeed, this is the most common description of these solutions. To uncover the underlying dependence of λ_e on experimental size ℓ , we employed a zero-dimensional model based on the FENE-P model to predict the evolution of the dimensionless filament diameter $a(\tau) = D(\tau)/D_0$, according to equations for mass and momentum balances (subscripts s and p denote, respectively, solvent and polymer), and microstructure evolution along the axial (z) and radial (r) directions,

$$\frac{Ec}{a} = \frac{3\beta}{1-\beta}E + f(A_{zz} - A_{rr}) \quad (2a)$$

$$\partial_\tau A_{zz} = (2E - f) A_{zz} + 1 \quad (2b)$$

$$\partial_\tau A_{rr} = (-E - f) A_{rr} + 1 \quad (2c)$$

$$\partial_\tau a = -\frac{aE}{2}, \quad (2d)$$

where we have introduced dimensionless time $\tau = t/\lambda$, elasto-capillary number $Ec = 2\lambda\gamma/\eta_p D_0$, solvent viscosity ratio $\beta = \eta_s/\eta_0$, dimensionless (time-varying) extensional strain rate $E = -2\lambda D^{-1} \frac{dD}{dt}$, the conformation tensor \mathbf{A} with rr and zz components, and the finite extensibility function $f = (b-3)/(b-A_{zz}-2A_{rr})$. By comparing

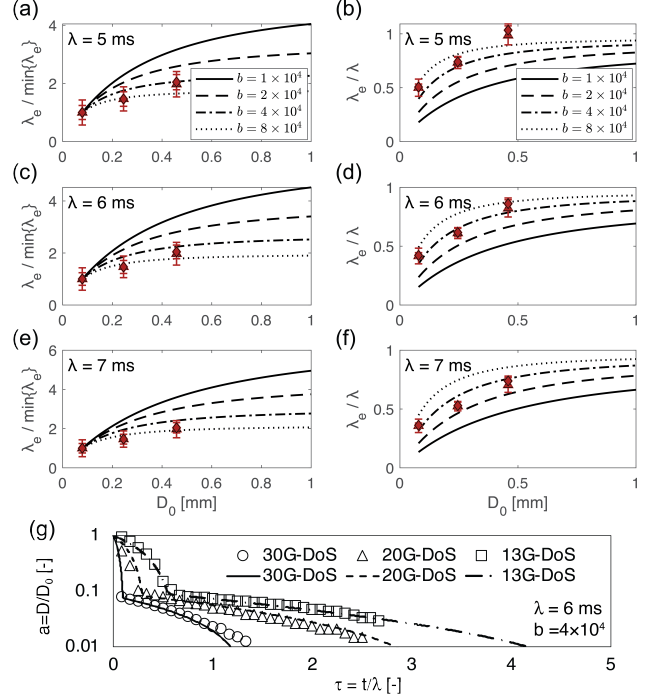


FIG. 3. Prediction of the relaxation time ratio $\lambda_e / \min\{\lambda_e\}$ (a, c, e) and relative ratio λ_e / λ (b, d, f) versus the initial diameter D_0 for the PEO-PEG-8M solution, assuming $\lambda = 5$ ms (a, b), 6 ms (c, d), and 9 ms (e, f), with varying extensibility $b \in \{2 \times 10^4, 4 \times 10^4, 8 \times 10^4\}$. The symbols represent experimental results of λ_e obtained from the dripping and DoS methods, suggesting a good approximation of $\lambda \approx 6$ ms and simultaneously indicating $b \approx 4 \times 10^4$ for the PEO-PEG solution. (g) Comparison of experimental and numerical results using $(\lambda, b) = (6 \text{ ms}, 4 \times 10^4)$ for three different diameter needles.

simplified analytical solutions (see [34] §IV-B1, B2), approximate solutions ([34] §IV-B3), and an analysis of the full model ([34] §IV-C1) under different assumptions, we demonstrated that the evolution is sensitive to the initial conformation $\mathbf{A}(t_1)$ for the EC stage. Only by solving the full model numerically can the variations in the VC, EC, and VC-EC transitions be captured accurately (see [34] §IV).

With the initial conditions $a = A_{rr} = A_{zz} = 1$, Eqs. (2) can be solved numerically ([34] §IV-C2) using MATLAB's ODE15s solver to yield the temporal evolution of the dimensionless diameter $a(\tau)$, conformation A_{zz} and A_{rr} , and extensional strain rate $E(\tau)$ (typical results are shown in Fig. 3 for $a(\tau)$; see also Fig. S10 for all variables). Based on the numerical results, we calculate the numerically predicted $\lambda_e / \lambda = \max\{2/(3E(t))\}$ for $t \geq t_1$, which corresponds to the early period of the EC stage (see [34], Fig. S10d), under various parameter choices of β , Ec , and b . This further allows the construction of a phase diagram of λ_e / λ as a function of the three parameters (see [34], Fig. S10e). Notably, every fixed β

enables the phase diagram to be approximated with a two-dimensional representation in terms of Ec and b (see [34], Fig. S10f).

For a specific viscoelastic liquid, as properties η_p , β and γ are measurable and size D_0 is controlled, we can assume a true relaxation time λ for determining Ec in Eq. (2a), and explore a wide range of b values in the numerical calculations. Taking the PEO-PEG solution as an example, numerical predictions of the relative ratio $\lambda_e/\min\{\lambda_e\}$ (Fig. 3a, c, e) and λ_e/λ (Fig. 3b, d, f) for assumed $\lambda \in \{5, 6, 7\}$ ms and $b \in \{10^4, 2 \times 10^4, 4 \times 10^4, 8 \times 10^4\}$ are compared with experimental results (symbols in Fig. 3). The trend of $\lambda_e/\min\{\lambda_e\}$ for different D_0 values provides a significant indicator for comparison with model predictions because both λ_e/λ and $\lambda_e/\min\{\lambda_e\}$ are uniquely determined for fixed Ec and β .

The comparisons of the two trends indicate that when $\lambda \approx 6$ ms, the numerical predictions align well with the experimental results (dash-dot curves in Fig. 3g). Furthermore, at the same time this analysis determines $b \approx 4 \times 10^4$. We emphasize that with this approach, only λ needs to be adjusted for comparison, while b is determined through the matching of the two trends. The comparison of experimental and numerical $a(\tau)$ shown in Fig. 3g suggests a good estimation for λ and b has been achieved. The same procedure was used to find a good agreement with the experimental data from [18] (Fig. S11 in [34]).

Next, we analyzed the experimental data presented in Fig. 2 and constructed a dimensionless phase diagram (note the logarithmic axes) of λ_e/λ as a function of Ec_e , b and β (Fig. 4a), where $Ec_e = 2\gamma\lambda_e/(D_0\eta_p)$, with each variable being directly measurable from experiments. Although different β values affect the map, particularly for small b , indicated in Fig. 4b, we can construct the phase diagram with all experimental data as shown in Fig. 4c; uncertainties in all measurable parameters were considered to determine the true relaxation time λ and the range of extensibility b for each viscoelastic fluid tested.

For the PEO-PEG-8M solution, the relaxation time is estimated as $\lambda \approx 6$ ms, with $b = 4 \times 10^{4 \pm 0.2}$. For the PEOvis solution, $\lambda \approx 150$ ms and $b = 2 \times 10^{4 \pm 0.1}$, consistent with the results from Ref. [18], where $b \approx 2 \times 10^4$ was estimated using an additional model. This agreement reinforces the validity of our approach. Furthermore, the larger b for PEO-PEG-8M compared to PEOvis aligns with their respective molecular weights, $M_w \sim 8 \times 10^6$ in our experiments versus $M_w \sim 4 \times 10^6$ in Ref. [18], given similar solvent mixtures (see [34], Tab. S1). This observation is further supported by the PEO-PEG-1M solution with $M_w \sim 1 \times 10^6$, which yields $(\lambda, b) \approx (2.2 \text{ ms}, 7 \times 10^{2 \pm 0.2})$.

For the PIB-PB-0.3 solution, experimental uncertainties prevent a precise determination of whether λ_e varies with D_0 , suggesting that a reasonable estimation of λ and b is not readily attainable. However, utilizing the

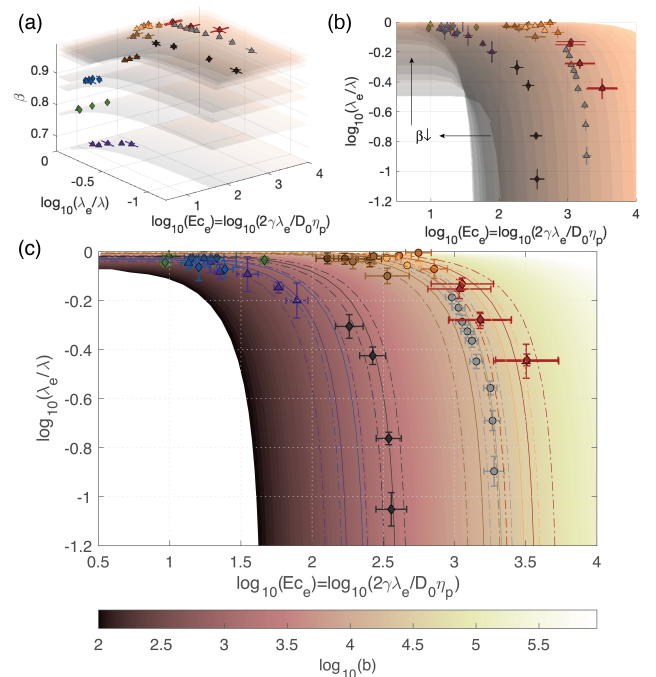


FIG. 4. Dimensionless map of the relaxation time ratio λ_e/λ versus the measurable elasto-capillary number $Ec_e = 2\gamma\lambda_e/(D_0\eta_p)$ for various unknown extensibility values $b \in [10^2, 10^6]$. (a) 3D maps for different β of a specific solution. (b) Top view of 3D maps. (c) Collapsed 2D map for easy comparison. The symbols represent experimental results (red: PEO-PEG-8M, purple: PEO-PEG-1M, green: PIB-PB-0.3, black: PIB-PB-0.02, blue: PS-DOP from current work, Ref. [18] (gray: PEOvis), and Ref. [33] (light/dark orange: PS16-50/100, light/dark brown: PS7-200/500)). Solid lines are obtained from fitting, with deviation ranges enclosed by dash-dot lines, suggesting the estimations.

more dilute PIB-PB-0.02 solution, we estimate $(\lambda, b) \approx (700 \text{ ms}, 2 \times 10^{3 \pm 0.1})$. Given that both solutions contain the same polymer at different dilutions, it is reasonable to assume that b remains unchanged. This leads to an inferred relaxation time of $\lambda \approx 850$ ms for PIB-PB-0.3.

From the phase diagram (Fig. 4), two distinct regions can be identified. When $\log_{10}(Ec_e^{-1}b) \gtrsim 1.5$, the experimentally measured λ_e becomes independent of the experimental size, i.e. $\lambda_e \sim \ell^0$. However, this does not imply that the true relaxation time λ is obtained. In this region, since b cannot be experimentally fitted, an additional evaluation of b is necessary to determine the specific value of λ_e/λ . In the region where $\log_{10}(\lambda_e/\lambda) \lesssim -0.6$, the slope of $\log_{10}(\lambda_e/\lambda)$ approaches infinity, indicating that $\lambda_e \sim D_0$. This is consistent with the scaling law $\lambda_e \sim \ell$ observed in Fig. 2 when $\ell(D_0)$ becomes sufficiently small. The $\lambda_e \sim \ell^{0.5}$ scaling law observed in Fig. 2 represents an empirical scaling behavior characterizing the transition between the two regions.

Thus, some predictions can be made. For fluids with

relatively low surface tension and strong viscoelasticity, such as PIB-PB-0.3 and PS-DOP, which exhibit $\log_{10}(Ec_e) \lesssim 1.5$ during capillary breakup, a size-independent exponential decay in the EC stage may occur. This implies that a nearly constant apparent relaxation time can be observed. In contrast, fluids with relatively high surface tension and low viscoelasticity, such as water-based dilute solutions like PEO-PEG and PEOvis, exhibit significant size dependence of the apparent relaxation time. The extensibility b determines the value of the critical Ec_e at which this effect occurs, with smaller b making this influence more readily triggered. Additionally, we speculate that in micro-scale capillary breakup processes (e.g., within biological tissues), where Ec_e is extremely big, the linear dependence of $\lambda_e \sim D_0 \sim \ell$ is likely to occur.

In summary, our study reveals, through experiments and numerical solutions, how inevitable pre-stretching during the visco-capillary stage of capillary breakup influences the exponential decay in the elasto-capillary stage and the apparent relaxation time λ_e obtained using classical formulations for viscoelastic fluids. Through a theoretical model, we demonstrate that the apparent relaxation time is always smaller than the actual relaxation time, i.e., $\lambda_e < \lambda$. We further identify that the size dependence of λ_e is governed by the extensibility b , solvent viscosity ratio β , and the dimensionless number $Ec_e = 2\gamma\lambda_e/(D_0\eta_p)$. Large b and small Ec_e result in size-independent behavior, while under big Ec_e conditions, the scaling $\lambda_e \sim D_0 \sim \ell$ emerges. We present a methodology for determining the actual relaxation time λ by synthesizing a series of apparent relaxation times λ_e measured under various size conditions. These findings provide a new perspective on accurately measuring viscoelastic properties using capillary breakup rheometry and offer insights into the size effects in the capillary breakup dynamics of viscoelastic fluids. Looking forward, several factors need to be considered to address the measurement of more complex fluids, such as those with shear-thinning viscosity, fluids where the IC stage dominates instead of the VC stage.

We thank Evgeniy Boyko for valuable discussions. We thank the NSF-supported project (NSF-BSF: Explaining the Mismatch of Experiments and Simulations for Viscoelastic Flows, 2246791) and the Princeton Materials Research Science and Engineering Center (MRSEC, DMR-2011750) for partially funding this work. J.H. acknowledges the Kwanjeong Educational Foundation Graduate Fellowship for financial support.

* nh0529@princeton.edu

† hastone@princeton.edu

[1] J. Eggers, *Rev. Mod. Phys.* **69**, 865–930 (1997).

- [2] G. H. McKinley, in *Rheology Reviews* (British Society of Rheology, Aberystwyth, 2005), pp. 1–49.
- [3] B. Keshavarz, E. C. Houze, J. R. Moore, M. R. Koerner, and G. H. McKinley, *Phys. Rev. Lett.* **117** (2016), 10.1103/physrevlett.117.154502.
- [4] V. Entov and E. Hinch, *J. Non-Newtonian Fluid Mech.* **72**, 31–53 (1997).
- [5] Y. Amarouchene, D. Bonn, J. Meunier, and H. Kellay, *Phys. Rev. Lett.* **86**, 3558–3561 (2001).
- [6] J. Eggers, M. A. Herrada, and J. H. Snoeijer, *J. Fluid Mech.* **887** (2020), 10.1017/jfm.2020.18.
- [7] A. Deblais, M. A. Herrada, J. Eggers, and D. Bonn, *J. Fluid Mech.* **904** (2020), 10.1017/jfm.2020.765.
- [8] C. Wagner, Y. Amarouchene, D. Bonn, and J. Eggers, *Phys. Rev. Lett.* **95** (2005), 10.1103/physrevlett.95.164504.
- [9] P. P. Bhat, S. Appathurai, M. T. Harris, M. Pasquali, G. H. McKinley, and O. A. Basaran, *Nat. Phys.* **6**, 625 (2010).
- [10] A. Deblais, K. Velikov, and D. Bonn, *Phys. Rev. Lett.* **120** (2018), 10.1103/physrevlett.120.194501.
- [11] E. Turkoz, J. M. Lopez-Herrera, J. Eggers, C. B. Arnold, and L. Deike, *J. Fluid Mech.* **851** (2018), 10.1017/jfm.2018.514.
- [12] L. E. Rodd, T. P. Scott, J. J. Cooper-White, and G. H. McKinley, *Appl. Rheol.* **15**, 12 (2005).
- [13] F. Ingremeau and H. Kellay, *Phys. Rev. X* **3** (2013), 10.1103/physrevx.3.041002.
- [14] V. Calabrese, A. Q. Shen, and S. J. Haward, *Macromolecules* **57**, 9668–9676 (2024).
- [15] S. L. Anna and G. H. McKinley, *J. Rheol.* **45**, 115–138 (2001).
- [16] G. H. McKinley and T. Sridhar, *Annu. Rev. Fluid Mech.* **34**, 375–415 (2002).
- [17] A. Aisling, R. Saraka, and N. J. Alvarez, *J. Non-Newtonian Fluid Mech.* **333**, 105321 (2024).
- [18] A. Gaillard, M. A. Herrada, A. Deblais, J. Eggers, and D. Bonn, *Phy. Rev. Fluids* **9** (2024), 10.1103/physrevfluids.9.073302.
- [19] J. Eggers and E. Villermaux, *Rep. Prog. Phys.* **71**, 036601 (2008).
- [20] A. M. Ardekani, V. Sharma, and G. H. McKinley, *J. Fluid Mech.* **665**, 46–56 (2010).
- [21] V. Sharma, S. J. Haward, J. Serdy, B. Keshavarz, A. Soderlund, P. Threlfall-Holmes, and G. H. McKinley, *Soft Matter* **11**, 3251 (2015).
- [22] B. Keshavarz, V. Sharma, E. C. Houze, M. R. Koerner, J. R. Moore, P. M. Cotts, P. Threlfall-Holmes, and G. H. McKinley, *J. Non-Newtonian Fluid Mech.* **222**, 171–189 (2015).
- [23] S. Rajesh, V. Thiévenaz, and A. Sauret, *Soft Matter* **18**, 3147–3156 (2022).
- [24] P. Bazazi, H. A. Stone, and S. H. Hejazi, *Phys. Rev. Lett.* **130** (2023), 10.1103/physrevlett.130.034001.
- [25] J. Dinic, L. N. Jimenez, and V. Sharma, *Lab Chip* **17**, 460 (2017).
- [26] J. Dinic, M. Biagioli, and V. Sharma, *J. Polym. Sci. Part B: Polym. Phys.* **55**, 1692–1704 (2017).
- [27] L. N. Jimenez, J. Dinic, N. Parsi, and V. Sharma, *Macromolecules* **51**, 5191 (2018).
- [28] K. Zinelis, T. Abadie, G. H. McKinley, and O. K. Matar, *Soft Matter* **20**, 8198–8214 (2024).
- [29] J. Dinic and V. Sharma, *Proc. Natl. Acad. Sci. USA* **116**, 8766 (2019).

- [30] O. Arnolds, H. Buggisch, D. Sachsenheimer, and N. Willenbacher, *Rheol. Acta* **49**, 1207 (2010).
- [31] J. Dinic, Y. Zhang, L. N. Jimenez, and V. Sharma, *ACS Macro Lett.* **4**, 804 (2015).
- [32] K. Zinelis, T. Abadie, G. H. McKinley, and O. K. Matar, *Soft Matter* **20**, 8198–8214 (2024).
- [33] V. Calabrese, A. Q. Shen, and S. J. Haward, “Effects of polydispersity and concentration on elastocapillary thinning of dilute polymer solutions,” (2024).
- [34] “Supplemental material,” See Supplemental Material at [URL] for additional rheological and experimental characterizations, as well as theoretical calculations.
- [35] C. Clasen, J. P. Plog, W.-M. Kulicke, M. Owens, C. Mascosko, L. E. Scriven, M. Verani, and G. H. McKinley, *Journal of Rheology* **50**, 849–881 (2006).
- [36] L. Campo-Deaño and C. Clasen, *Journal of Non-Newtonian Fluid Mechanics* **165**, 1688–1699 (2010).

Supporting Information for “Revealing Actual Viscoelastic Relaxation Time in Capillary Breakup”

Nan Hu,^{1,*} Jonghyun Hwang,¹ Tachin Ruangkriengsin,² and Howard A. Stone^{1,†}

¹*Department of Mechanical and Aerospace Engineering, Princeton University, NJ 08544, USA*

²*Program in Applied and Computational Mathematics, Princeton University, NJ 08544, USA*

CONTENTS

I. Existed data of CaBER method	1
II. Viscoelastic Liquid Preparation, Characterization and Selection	1
III. Experimental Setup and Procedure	2
IV. Analytical Model and Numerical Results	4
A. Zero-dimensional Model	4
B. Simplified Analytical Solutions	5
1. Infinite extensibility length, i.e., $b = \infty$	5
2. Finite extensibility b with unknown $A_{zz}(t_1)$	6
3. Piecewise Approximation Considering Pre-Stretching	6
C. Full model	8
1. Analytical analysis	8
2. Numerical results	9
3. Determine actually relaxation time	9
V. Estimation of filament diameter D_0 in breakup for dripping and DoS method	9
References	9

I. EXISTED DATA OF CABER METHOD

Gaillard et al. [1] measured the capillary breakup process of PEOvis solutions, i.e., polyethylene oxide polymer with $M_w = 4 \times 10^6$ in a water-polyethylene glycol ($M_w = 2 \times 10^4$) mixture, using the quasi-steady separating CaBER method between parallel plates of different diameters $\ell \in \{2, 3.5, 5, 7, 10, 15, 25\}$ mm (see Fig. S1a). The detailed measurement data were redrawn in Fig. S1(b). Notably, the initial diameter of the liquid column, D_0 , is not equal to ℓ , but a linear relationship exists as shown in Fig. S1(c) from their experimental results. The specific physical properties of the PEOvis solution are viscosity $\eta_0 = 0.248 \pm 0.001$ Pa s, solvent viscosity $\eta_s = 0.246 \pm 0.001$ Pa s ($\beta = \eta_s/\eta_0 = 0.988 \pm 0.006$), and surface tension $\gamma = 56$ mN/m.

Calabrese et al. [2] also have measured dilute polymeric solutions of polystyrene (PS) dissolved in dioctyl phthalate (DOP), with two average molecular weights $M_w \approx 7 \times 10^6$ and 1.6×10^7 (labeled as PS7 and PS16). Four specific solutions named as PS16-100, PS16-50,

PS7-500, and PS7-200 are adopted in the analysis, corresponding to concentrations of 100, 50, 500, and 200 ppm. The related parameters are listed as: $\ell \in \{4, 6, 8\}$ mm, $\eta_s \approx 57$ mPa s, $\gamma \approx 31$ mN/m, and $\eta_p \approx \{2, 2, 7, 3\}$ mPa s for PS16-100, PS16-50, PS7-500, and PS7-200. Extensibility $b = 3.2 \times 10^4$ and 1.36×10^4 from [2] are adopted in the full model analysis.

II. VISCOELASTIC LIQUID PREPARATION, CHARACTERIZATION AND SELECTION

PEO-PEG Solution Preparation: First, 60 wt.% deionized water was weighed, followed by adding 40 wt.% of polyethylene glycol (PEG, average $M_w = 8000$ g/mol, Aladdin). The mixture was stirred using a magnetic stirrer at room temperature for 24 hours until fully dissolved. Then, polyethylene oxide polymer (PEO, Sigma-Aldrich) was added and stirred for another 24 hours. Three different molecular weight PEOs were used including $M_w = 8 \times 10^6$, 1×10^6 and 1×10^5 , denoted as 8 M, 1 M and 0.1 M, respectively. Since the critical concentration c^* has been well investigated [3], the Mark-Houwink relation as intrinsic viscosity $[\eta] = 0.072M_w^{0.65}$ was adopted, suggesting the critical concentration $c^* = 0.047$ wt.%, 0.195 wt.% and 0.93 wt.% for 8 M, 1 M and 0.1 M, respectively. Hence, the corresponding concentration of PEO is 0.04 wt.%, 0.19 wt.%, and 0.93 wt.%, respectively. The solution was re-stirred before each measurement and used within two weeks after preparation to avoid degradation effects.

PIB-PB Solution Preparation: We first prepared a 3 wt.% polyisobutylene (PIB) solution by melting and dissolving the PIB polymer (average $M_w = 4.2 \times 10^6$, Sigma-Aldrich) in light mineral oil (Sigma-Aldrich) at 100°C with heating and stirring. Next, we mixed polybutene (PB, average $M_n = 2300$, Sigma-Aldrich) and light mineral oil as the solvent, to which the previously prepared PIB-mineral oil solution was added. The final solution, containing 0.4, 0.3, 0.2, 0.02 wt.% PIB polymer with 60 wt.% PB and 40 wt.% light mineral oil as the solvent, was obtained through mechanical stirring followed by vacuum degassing.

PS-DOP Solution Preparation: Polystyrene (PS, average $M_w = 2 \times 10^6$ g/mol, Sigma-Aldrich) was dissolved in dioctyl phthalate (DOP, Sigma-Aldrich) at a mass fraction of 0.1%. The mixture was stirred until fully dissolved. Notably, PS-DOP is known to be a theta system

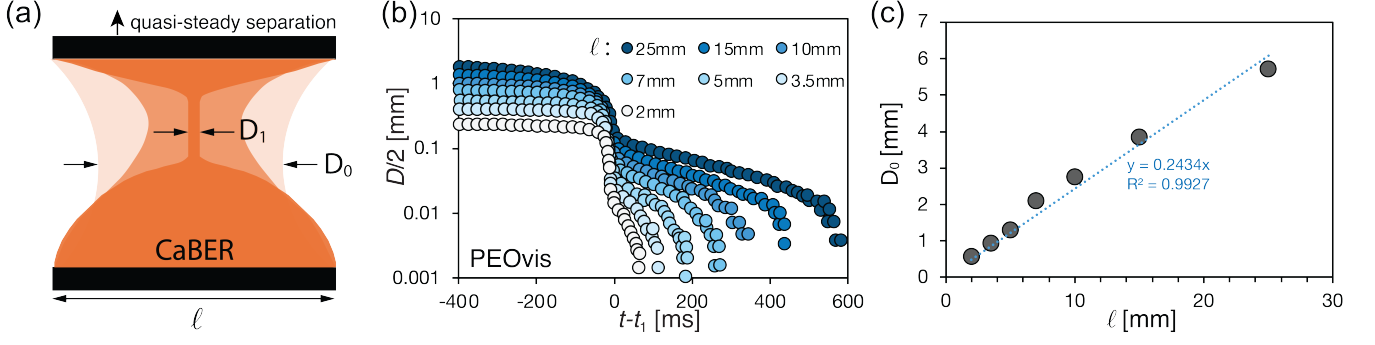


Fig. S1. Experiments on the CaBER method with flat plates of varying diameter. (a) Schematic of the stepwise plate separation CaBER method, designed to maintain the liquid bridge in a quasi-steady state prior to capillary breakup. (b) Evolution of the liquid bridge neck radius $R = D/2$, as a function of time for different plate diameters ℓ , using a PEOvis solution (reproduced from Ref. [1] with the permission of American Physical Society). The time t_1 marks the onset of the elastic-capillary stage. (c) Dependence of the initial neck diameter D_0 on the plate diameter ℓ in experiments. The dotted line represents the linear fit $D_0 \approx 0.24\ell$ for PEOvis in the quasi-steady separation CaBER method.

at 22°C [4]. The solution was further diluted stepwise by adding DOP to prepare samples with mass fractions of 0.05 wt.% and 0.025 wt.%.

The viscosity and modulus for each solution was measured using a rheometer (Anton Paar 302e). For viscosity testing, a cone-and-plate configuration was used (cone angle $\alpha = 1^\circ$, plate radius $R = 25$ mm) for PS-DOP and PIB-PB solutions, while a double-gap configuration was used (DG26.7) for PEO-PEG solutions so as to prevent evaporation effects. The results, shown in Fig. S2(a,d,h), indicate that the viscosity of solutions remains nearly constant with varying shear rates, suggesting that they can be considered as Boger fluids. Measured specific viscosity $\eta_{sp} = (\eta_0 - \eta_s)/\eta_0$ validated that all PS-DOP (Fig. S2b) and PIB-PB solutions (Fig. S2e) remain within the dilute regime due to $\eta_{sp} \sim c$. Here we choose and label 0.05 wt.% PS solution as PS-DOP, 0.3 wt.% PIB solution as PIB-PB-0.3, and 0.02 wt.% PIB solution as PIB-PB-0.02 for the test fluids.

Using the same configuration settings, small-amplitude oscillatory rheology tests were conducted to measure the loss modulus (G'') and storage modulus (G'). The results are shown in Fig. S2(c,f,g,i), corresponding to the PS-DOP, PIB-PB-0.3, PIB-PB-0.02, and PEO-PEG solutions, respectively. In Fig. S2(c), the curves were fitted using the Zimm model, while in Fig. S2(f,g), the curves were fitted using the Oldroyd-B model. The formulas for the moduli under small-amplitude oscillation for the Oldroyd-B model are:

$$G'(\omega) = \frac{G_p \lambda_s^2 \omega^2}{1 + (\lambda_s \omega)^2} \quad (\text{S1a})$$

$$G''(\omega) = \eta_s \omega + \frac{G_p \lambda_s \omega}{1 + (\lambda_s \omega)^2}. \quad (\text{S1b})$$

For the Zimm model the equations are:

$$G'(\omega) = G_p \frac{\omega \lambda_s \sin[\chi \operatorname{atan}(\omega \lambda_s)]}{\left[1 + (\omega \lambda_s)^2\right]^{\chi/2}}, \quad (\text{S2a})$$

$$G''(\omega) = \eta_s \omega + G_p \frac{\omega \lambda_s \cos[\chi \operatorname{atan}(\omega \lambda_s)]}{\left[1 + (\omega \lambda_s)^2\right]^{\chi/2}}, \quad (\text{S2b})$$

where ω is the frequency, λ_s is the relaxation time for small-amplitude-oscillatory-shear rheometry, $G_p = \eta_p/\lambda$, and $\chi = 1/3$ at the theta temperature [5].

The surface tension of all studied liquids was measured using the pendant drop method based on the initial droplet shape in the dripping tests. The physical property data for all tested fluids are summarized in the Table I.

III. EXPERIMENTAL SETUP AND PROCEDURE

The experimental setup for capillary breakup tests used in this study is shown in Fig. S3(a). The system consists of a high-speed camera (640L, Phantom), microscope objectives (2X, 5X, and 10X, Nikon, to accommodate different needle diameters), a syringe pump (Harvard 2000), an LED backlight source (130,000 LUX, PHLOX), and a custom-made transparent chamber. As illustrated in the schematics shown in Figs. S3(b) and (c), both the needle and microscope objective are positioned inside the transparent chamber for the dripping and DoS tests. The sealed chamber prevents environmental airflow from disturbing the filament during capillary breakup. Additionally, a liquid reservoir containing the test fluid is placed inside the chamber. Before each test,

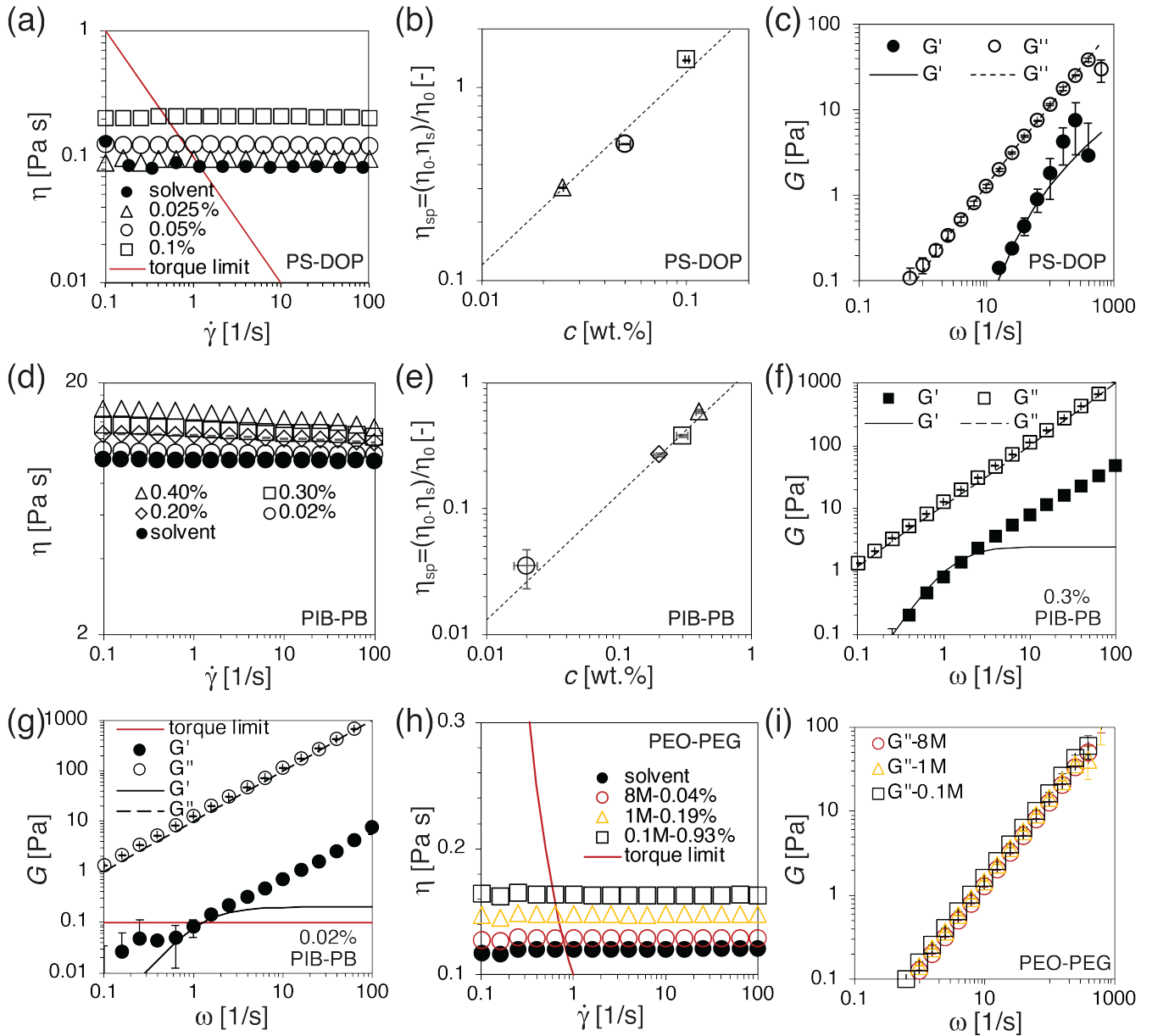


Fig. S2. Rheological characterization of the test fluids, including PS-DOP solutions (a–c), PIB-PB solutions (d–g), and PEO-PEG solutions (h–i). (a) Viscosity η as a function of shear rate $\dot{\gamma}$ at various concentrations for PS-DOP (a), PIB-PB (d), and PEO-PEG (h) solutions. (b) Specific viscosity, defined as $\eta_{sp} = (\eta_0 - \eta_s)/\eta_s$, versus concentration c , where a power-law exponent of 1 indicates the dilute regime. (c) Measurement of the loss modulus (G'') and storage modulus (G') under small-amplitude oscillatory shear for PS-DOP at $c = 0.05$ wt.% (c), PIB-PB at $c = 0.3$ wt.% (f) and $c = 0.02$ wt.%, and PEO-PEG with various molecular weights of PEO (i). In all figures, the absence of error bars indicates that the error bars are smaller than the symbol size. The curves in (c) are fitted using the Zimm model, while those in (f, e) are fitted using the Oldroyd-B model.

the chamber is allowed to equilibrate for several hours, ensuring the space is saturated with the solvent vapor of the test liquid, thereby minimizing the effects of evaporation during the experiment.

Standard syringe needles were used as nozzles in the experiments, with models including {30G, 25G, 20G, 15G, 13G}, corresponding to outer diameters $\ell \in \{0.305, 0.508, 0.902, 1.829, 2.413\}$ mm. The con-

trolled flow rate during the experiments was set to $Q = 1 - 10 \mu\text{L}/\text{min}$ to ensure that the hanging droplet extruded from the nozzle remained quasi-static, avoiding pre-stretching of the polymer induced by injection. The images capturing the liquid thinning and breakup processes were batch-processed using a custom MATLAB program. This program was used to track the liquid interface and extract the temporal evolution of the min-

TABLE I. Summary of physical property data for the fluids used in this study. Viscosity η_0 and solvent viscosity η_s , viscosity ratio $\beta = \eta_s/\eta_0$, and surface tension γ are reported. Fitting relaxation time λ_s based on Oldroyd-B model or Zimm model from small amplitude oscillatory shear rheometry.

Name	η_0 [Pa s]	η_s [Pa s]	β	γ [mN/m]	λ_s [s]
PIB-PB-0.3	12.88 ± 0.08	9.95 ± 0.04	0.773 ± 0.006	28.56 ± 1.18	0.7 ± 0.1
PIB-PB-0.02	10.22 ± 0.01	9.95 ± 0.04	0.974 ± 0.004	29.55 ± 1.62	0.7 ± 0.1
PS-DOP	0.124 ± 0.001	0.081 ± 0.001	0.653 ± 0.010	31.78 ± 3.14	0.030 ± 0.002
PEO-PEG-8M	0.128 ± 0.001	0.127 ± 0.001	0.985 ± 0.011	50.26 ± 2.10	/
PEO-PEG-1M	0.148 ± 0.001	0.127 ± 0.001	0.858 ± 0.009	46.62 ± 1.50	/

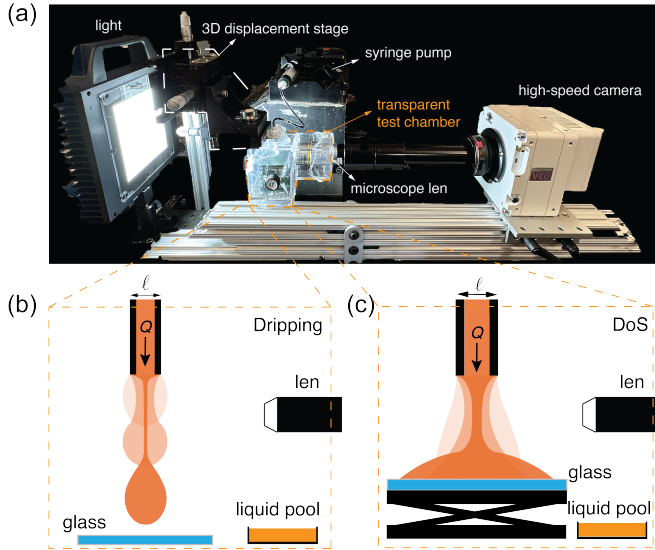


Fig. S3. Experimental setup and schematic diagrams of dripping and DoS methods. (a) The capillary breakup testing apparatus consists of a high-speed camera equipped with a microscope objective, a syringe pump, a three-dimensional displacement stage, and a light source. A transparent testing chamber is used to prevent environmental airflow disturbances and to reduce evaporation of the test liquid. (b) Schematic of the dripping method. (c) Schematic of the DoS method, where the substrate is made of quartz glass. A liquid reservoir inside the chamber is included to create a saturated vapor atmosphere.

imum diameter $D(t)$. Representative results from the dripping and DoS tests on PEO-PEG, PIB-PB, and PS-DOP solutions are presented in Fig. 1 of the main text and Figs. S4. Each test was repeated three times to ensure the reproducibility of the $D(t)$ data.

IV. ANALYTICAL MODEL AND NUMERICAL RESULTS

When the droplet or liquid bridge is stretched beyond the critical condition for the Rayleigh-Plateau instability, the break-up process will be dominated by viscous, capillary, and inertial forces for Newtonian fluids, which can be categorized as visco-capillary (VC) or inertial-

capillary (IC) regimes depending on the Ohnesorge number ($Oh \equiv \eta/\sqrt{\rho R \gamma}$) according to $Oh \gg 1$ or $Oh \ll 1$ respectively, where η , ρ , γ represent viscosity, density, and surface tension. R is the characteristic size of the droplet or liquid bridge.

The physical principle of capillary breakup rheometry for a viscoelastic fluid is based on the elasto-capillary (EC) dynamics of the liquid bridge/filament after IC or VC. There is a widely-used formula in numerous papers to calculate relaxation time λ as

$$\frac{R(t)}{R_1} = \left(\frac{G_p R_1}{2\gamma} \right)^{1/3} \exp \left[\frac{-(t - t_1)}{3\lambda} \right], \quad (S3)$$

where $R(t)$ is the minimum radius of filament, $G_p \equiv \eta_p/\lambda$ modulus of viscoelastic fluids, t_1 is the onset of the EC regime, and R_1 is the radius at this time. However, there are some intrinsic problems about this formula as given in the following discussion.

A. Zero-dimensional Model

Consider a cylindrical liquid filament with radius R and length L in the axisymmetric coordinate of (r, z) . The time-dependent relationship between R and L in cylinder deformation is

$$\pi R^2 L = \pi (R + \dot{R} \Delta t)^2 (L + \dot{L} \Delta t) \Rightarrow \dot{\epsilon} \equiv \frac{\dot{L}}{L} = -\frac{2}{R} \dot{R}, \quad (S4)$$

where $\dot{R} \equiv dR/dt$, $\dot{L} \equiv dL/dt$, Δt is a differential time, and $\dot{\epsilon}$ is the extensional strain rate. The velocity field in the filament thinning flow can be considered as $(v_r, v_z) = (-r\dot{\epsilon}/2, z\dot{\epsilon})$. Hence, the momentum equation neglecting inertial effects for $Oh \gg 1$ is

$$-\frac{\gamma}{R} = \sigma_{rr} = -p - \eta_s \dot{\epsilon} + \sigma_{p,rr} \quad (S5a)$$

$$0 = \sigma_{zz} = -p + 2\eta_s \dot{\epsilon} + \sigma_{p,zz}, \quad (S5b)$$

where σ is the stress and subscript p is the polymeric part. The combination of the above two equations leads to

$$\frac{\gamma}{R} = 3\eta_s \dot{\epsilon} - \sigma_{p,rr} + \sigma_{p,zz}. \quad (S6)$$

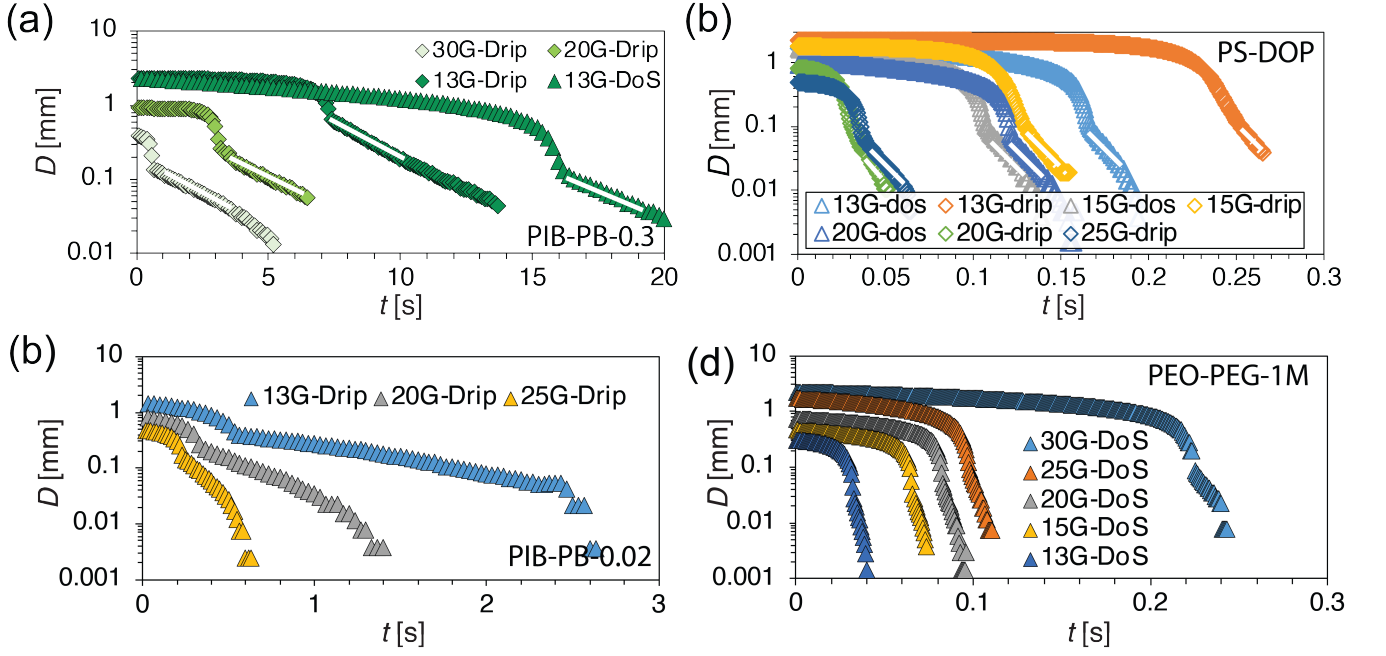


Fig. S4. Representative experimental results of filament diameter evolution over time for (a) PIB-PB-0.3, (b) PS-DOP, (c) PIB-PB-0.02, and (d) PEO-PEG-1M solutions.

Based on the FENE-P model, the polymeric stress σ_p can be written as [6]

$$\sigma_p = \frac{\eta_p}{\lambda} (f\mathbf{A} - \mathbf{I}) = \frac{\eta_p}{\lambda} \left(\frac{b-3}{b - \text{tr}(\mathbf{A})} \mathbf{A} - \mathbf{I} \right) \quad (\text{S7})$$

where $\text{tr}(\mathbf{A})$ denotes the trace of the conformation tensor \mathbf{A} and b is the extensibility parameter. If $f = 1$, Eq. (S7) will reduce to the Oldroyd-B model, i.e. $b = \infty$. The conformation tensor \mathbf{A} obeys

$$\overset{\nabla}{\mathbf{A}} = -\frac{1}{\lambda} (f\mathbf{A} - \mathbf{I}), \quad (\text{S8})$$

where $\overset{\nabla}{\mathbf{A}} \equiv \partial_t \mathbf{A} + (\mathbf{v} \cdot \nabla) \mathbf{A} - (\nabla \mathbf{v}) \cdot \mathbf{A} - \mathbf{A} \cdot (\nabla \mathbf{v})^T$ is the upper convected derivative of the conformation tensor. Substitution of the flow field (v_r, v_z) into (S8) and combining with the momentum equation yields

$$\frac{\gamma}{R} = 3\eta_s \dot{\epsilon} + \frac{\eta_p}{\lambda} f (A_{zz} - A_{rr}) \quad (\text{S9a})$$

$$\lambda \dot{A}_{zz} = (2\dot{\epsilon}\lambda - f) A_{zz} + 1 \quad (\text{S9b})$$

$$\lambda \dot{A}_{rr} = -(\dot{\epsilon}\lambda + f) A_{rr} + 1 \quad (\text{S9c})$$

$$f = \frac{b-3}{b - A_{zz} - 2A_{rr}} \quad (\text{S9d})$$

$$\dot{\epsilon} = -2 \frac{\dot{R}}{R}. \quad (\text{S9e})$$

This set of equations describes the variations of radius $R(t)$, extensional strain rate $\dot{\epsilon}(t)$, and conformation components $A_{zz}(t)$ and $A_{rr}(t)$ as a function of time t .

B. Simplified Analytical Solutions

1. Infinite extensibility length, i.e., $b = \infty$

Adopting assumptions of (i) $f = 1$ for infinite b and (ii) $A_{zz} \gg 1$, we can obtain an ODE for A_{zz}

$$\dot{A}_{zz} = 2\dot{\epsilon} A_{zz} - \frac{1}{\lambda} A_{zz} = -\frac{4\dot{R}}{R} A_{zz} - \frac{1}{\lambda} A_{zz}, \quad (\text{S10})$$

for which the time-dependent solution $A_{zz}(t)$ with the initial conditions $A_{zz}(t_1) = 1$ and $R(t_1) = R_1$ is

$$A_{zz} = \frac{R_1^4}{R^4(t)} \exp\left(-\frac{t-t_1}{\lambda}\right). \quad (\text{S11})$$

Substituting (S11) into (S9a) with two other assumptions of (iii) negligible viscous effects, $\sigma_s \equiv 3\eta_s \dot{\epsilon} \ll \sigma_{p,zz}$, and (iv) $A_{zz} \gg A_{rr}$ (implying $\sigma_{p,zz} \gg \sigma_{p,rr}$), the final formula for $R(t)$ is

$$\frac{R(t)}{R_1} = \left(\frac{\eta_p R_1}{\lambda \gamma} \right)^{1/3} \exp\left(\frac{t_1 - t}{3\lambda}\right). \quad (\text{S12})$$

Hence, the extensional strain rate $\dot{\epsilon}$ and A_{zz} during EC is

$$\dot{\epsilon} = -2\dot{R}/R = \frac{2}{3\lambda} \quad (\text{S13})$$

$$A_{zz} = \left(\frac{GR_1}{\gamma} \right)^{-4/3} \exp\left(\frac{t-t_1}{3\lambda} \right). \quad (\text{S14})$$

This formula was first derived by Entov and Hinch [7] in 1997. Defining the Deborah number $De \equiv \epsilon\lambda$, we can find a constant $De = 2/3$ in the EC regime as derived as

$$De = \epsilon\lambda = -\frac{2\dot{R}}{R}\lambda = \frac{2}{3}. \quad (\text{S15})$$

However, it is well-known that the Oldroyd-B model fails to provide the correct prediction of polymer extension for $De > 1/2$ (the coil-stretch transition). Thus, there is inconsistency.

2. Finite extensibility b with unknown $A_{zz}(t_1)$

With the same assumptions (ii) $A_{zz} \gg 1 > A_{rr}$ and (iii) $\sigma_p \gg \sigma_s$, and assuming (v) b is finite and $b \gg 3$ for the EC regime, we can derive

$$\frac{\gamma}{R} = \frac{\eta_p}{\lambda} f A_{zz} \Rightarrow R = \frac{\gamma\lambda}{\eta_p} \left(\frac{1}{A_{zz}} - \frac{1}{b} \right). \quad (\text{S16})$$

Therefore, we obtain

$$\dot{R} = -\frac{\gamma\lambda}{\eta_p} \frac{\dot{A}_{zz}}{A_{zz}^2} \Rightarrow \dot{\epsilon} = \frac{2\dot{A}_{zz}}{A_{zz}(1 - A_{zz}/b)}. \quad (\text{S17})$$

Substituting (S17) into (S9b) yields

$$\frac{A_{zz}}{\lambda} = \dot{A}_{zz} \left(3 + \frac{A_{zz}}{b} \right), \quad (\text{S18})$$

which has an implicit solution, also as reported in [1], given by

$$\frac{t-t_1}{\lambda} = \frac{A_{zz} - A_{zz,1}}{b} + 3 \ln \left(\frac{A_{zz}}{A_{zz,1}} \right), \quad (\text{S19})$$

where the subscript 1 represents the onset of EC, and $A_{zz,1}$ denotes the stretching state at that time. Recalling (S16) and taking the logarithm of both sides of the equation, we obtain

$$\log_{10}(R/R_1) = \log_{10} \left(\frac{1}{A_{zz}} - \frac{1}{b} \right) + \log_{10} \left(\frac{\gamma\lambda}{\eta_p R_1} \right) \quad (\text{S20})$$

The numerical results of (S20) are shown in Figure S5a. By taking the tangent line at the initial point for fitting based on the Oldroyd-B model, it indicates that the fitting relaxation time $\lambda_{f,OB}$ is always less than the true relaxation time λ and decreases with increasing $A_{zz,1}$ (Figure S5b).

Although this implicit expression captures the reduction of the apparent relaxation time due to finite extensibility b , the inability to determine the initial value $A_{zz,1}$ in the EC phase introduces a new fitting parameter $A_{zz,1}$ if this expression is used to interpret experimental data.

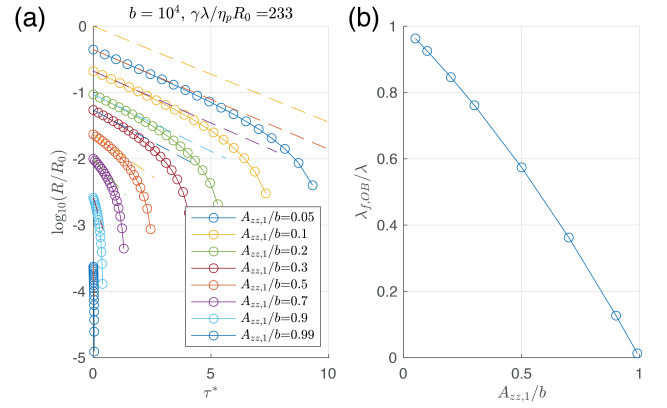


Fig. S5. (a) Filament radius R evolves at various pre-stretched conditions of $A_{zz,1}$ and (b) corresponding fitting $\lambda_{f,OB}$

3. Piecewise Approximation Considering Pre-Stretching

One approach to account for the pre-stretching process is to treat the VC and EC stages separately, i.e. “piecewise approximation”, using the endpoint of the VC stage as the initial condition for the EC stage. A natural way to implement this is to determine the transition point based on the relative magnitudes of the polymeric stress σ_p and the viscous stress σ_s [8]. Below, we demonstrate how to derive the corresponding approximate formula based on this method. If $3\eta_s\dot{\epsilon} \gg \sigma_{p,zz} - \sigma_{p,rr}$, the Eq. (S9a) simplifies to:

$$\gamma/R = 3\eta_s\dot{\epsilon} \Rightarrow R = (t_c - t)\gamma/6\eta_s, \quad (\text{S21})$$

where $t_c = 6\eta_s R_0/\gamma$. Although the elastic force has a minor influence during the VC regime, the polymer stretches along with the transient extensional strain rate, $\dot{\epsilon} = 2/(t_c - t)$. Then substituting $\dot{\epsilon} = 2/(t_c - t)$ into (S9b) yields

$$\partial_\tau A_{rr} = - \left(\frac{2}{\tau_c - \tau} + f \right) A_{rr} + 1 \quad (\text{S22a})$$

$$\partial_\tau A_{zz} = \left(\frac{4}{\tau_c - \tau} - f \right) A_{zz} + 1, \quad (\text{S22b})$$

where $\tau = t/\lambda$ and $\tau_c = t_c/\lambda = 6\eta_s R_0/\gamma\lambda$ in the EC regime, and $f = (b-3)/(b - \text{tr} \mathbf{A})$ for the FENE-P model or $f = 1$ for the Oldroyd-B model. This set of equations cannot be solved analytically for $\text{tr} \mathbf{A}$.

A typical estimate gives $\mathcal{O}(\tau_c) \in [0.01, 1]$ for dilute water-based polymer solutions, where $\eta_s \in [10^{-2}, 10^{-1}]$ Pa-s, $\gamma \in [30, 70]$ mN-m, $\lambda \in [10, 100]$ ms, and $R_0 \in [0.3, 3]$ mm. This set of equations can be solved numerically with the initial condition $\mathbf{A} = \mathbf{I}$. Furthermore, we can estimate $A_{zz}(t)$ using the Oldroyd-B model. The

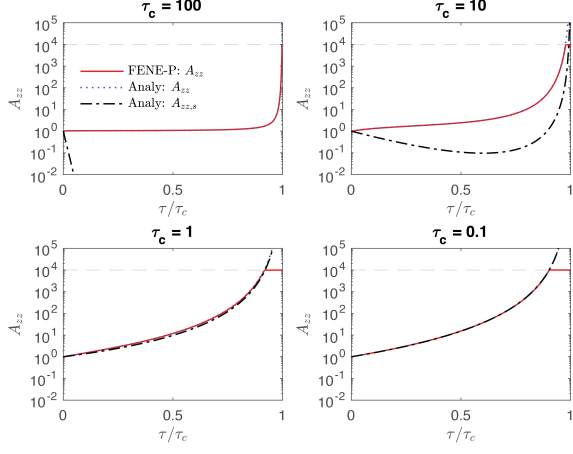


Fig. S6. Transient components of $\mathbf{A}(t)$ in IC or VC regime for various τ_c when $\beta = 0.9$ and $b = 10^4$

analytical solution for $f = 1$ is

$$A_{zz}(\tau) = \frac{e^{-\tau}}{(\tau_c - \tau)^4} \left[-24 + e^\tau (\tau_c^4 + 24 - 24\tau + 12\tau^2 - 4\tau^3 + 4\tau_c^3 (1 + e^\tau (\tau - 1)) + 6\tau_c^2 (-2 + e^\tau (2 - 2\tau + \tau^2)) - 4\tau_c (6 + e^\tau (-6 + 6\tau - 3\tau^2 + \tau^3))) \right] \quad (\text{S23a})$$

$$A_{rr}(\tau) = \frac{e^{-\tau}(\tau_c - \tau)}{\tau_c^2} \left[(\tau_c - \tau) + \tau_c^2 + \tau_c^2 e^\tau - \tau + \tau_c \tau - \tau_c^2 e^{\tau_c} (\tau_c - \tau) \text{Ei}(-\tau_c) + \tau_c^2 e^{\tau_c} (\tau_c - \tau) \text{Ei}(-\tau_c + \tau) \right], \quad (\text{S23b})$$

where the integral function $\text{Ei}(x) = -\int_{-x}^{\infty} \frac{e^{-t}}{t} dt$. If $4/\tau_c \gg 1$ so that f may be neglected in the Eq.(S22), these equations can be further simplified as

$$A_{zz,s}(\tau) = \frac{\tau_c^4 \exp(-\tau)}{(\tau_c - \tau)^4} \quad (\text{S24a})$$

$$A_{rr,s}(\tau) = A_{\theta\theta,s}(\tau) = \frac{(\tau_c - \tau)^2 \exp(-\tau)}{\tau_c^2}. \quad (\text{S24b})$$

Eq.(S24a) has been reported in [8]. The numerical and analytical results of the A_{zz} variation are displayed in Fig. S6, which indicates that A_{zz} predicted by the Oldroyd-B model can overlap with the FENE-P model before reaching a plateau.

With the obtained A_{rr} and A_{zz} , we can evaluate the ratio of transient polymeric stress $\sigma_{p,zz} - \sigma_{p,rr}$ to viscous stress $3\eta_s \dot{\epsilon}$ by denoting $\xi \equiv (\sigma_{zz} - \sigma_{rr})/\sigma_s = \eta_p (f A_{zz} -$

$f A_{rr})/3\eta_s \dot{\epsilon}$, or

$$\xi = \frac{1 - \beta}{3\beta} f \frac{A_{zz} - A_{rr}}{\dot{\epsilon}(\tau)} = \frac{1 - \beta}{6\beta} f (A_{zz} - A_{rr})(\tau_c - \tau). \quad (\text{S25})$$

Considering $A_{rr} \ll A_{zz}$ in the late stage shown in Fig. S6, we find the asymptotes ξ_{zz} as

$$\xi_{zz} = \frac{1 - \beta}{6\beta} \frac{b - 3}{b - A_{zz}} A_{zz} (\tau_c - \tau), \quad \text{for } A_{zz} \gg A_{rr}, \quad (\text{S26a})$$

$$\xi_{zz,s} = \frac{1 - \beta}{6\beta} \frac{\tau_c^4 \exp(-\tau)}{(\tau_c - \tau)^3}, \quad \text{for } A_{zz} \gg A_{rr} \text{ and } \tau_c \ll 4. \quad (\text{S26b})$$

The numerical and analytical results of ξ for $\beta = 0.9$ and $b = 10^4$ are depicted in Fig. S7.

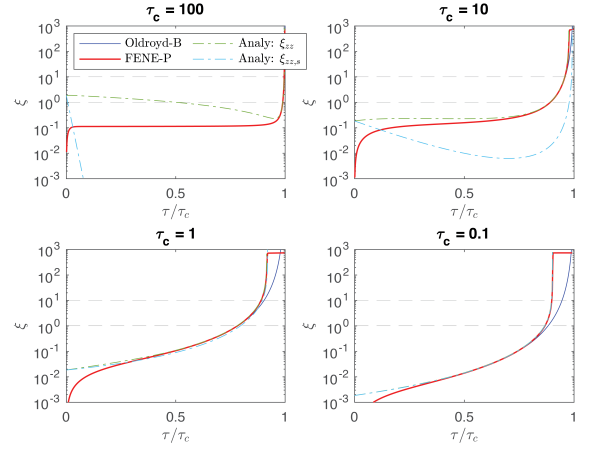


Fig. S7. Ratio of transient polymeric stress $\sigma_{p,zz} - \sigma_{p,rr}$ to viscous stress $3\eta_s \dot{\epsilon}$ with the definition $\xi = (\sigma_{zz} - \sigma_{rr})/\sigma_s$

Wagner et al. [8] suggested a threshold (denoted with $*$) by letting $\partial_{\tau^*} A_{zz}^* = 0$, which leads to

$$0 = 2\dot{\epsilon}^* \lambda A_{zz}^* - (f^* A_{zz}^* - 1) \quad (\text{S27a})$$

$$3\eta_s \frac{2}{\lambda(\tau_c - \tau^*)} = 3\eta_s \dot{\epsilon}^* + \frac{\eta_p}{\lambda} f^* (A_{zz}^* - A_{rr}^*) \quad (\text{S27b})$$

Hence, the τ^* can be numerically determined from

$$\frac{A_{zz}^*}{b} = \frac{\frac{4}{\tau_c - \tau^*} - 1}{\frac{4}{\tau_c - \tau^*} + \frac{2b\eta_p}{3\eta_s}}. \quad (\text{S28})$$

It should be emphasized that (S24a) was adopted to obtain the τ^* in (S28) instead of (S23a) in the work of [8], which is limited by the assumption of $\tau_c \ll 4$. Furthermore, the later results of the full model in Section §IV-C show that the $\partial_{\tau^*} A_{zz}^* = 0$ never occurs.

In order to consider a range of τ_c from 10^{-3} to 10^2 , we here substitute (S23a) into the above equation to numerically obtain τ^* and A_{zz}^* , which is also compared with

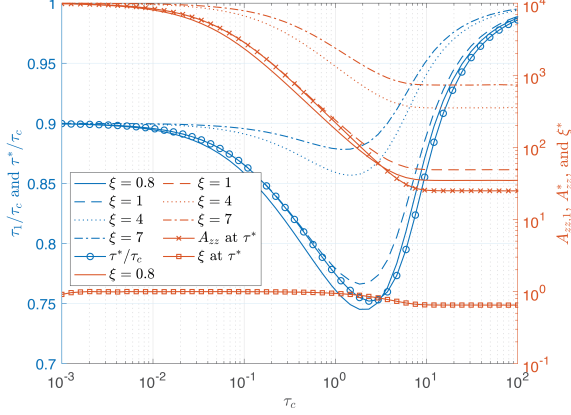


Fig. S8. Relative transition time τ_{ec}/τ_c and corresponding $A_{zz,1}$ for various τ_c under different thresholds of ξ .

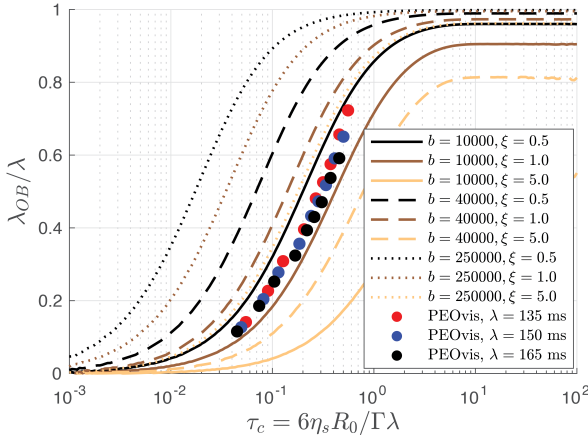


Fig. S9. Relationship of $\lambda_{f,OB}/\lambda$ with τ_c for $b \in \{10^4, 4 \times 10^4, 2.5 \times 10^5\}$ and $\xi \in \{0.5, 1, 5\}$. Markers are experimental results of PEOvis [1] by assuming $\lambda \in \{135, 150, 165\}$ ms.

results from cases of fixing ξ to determine τ_{ec} and $A_{zz,1}$, as shown in Fig. S8. It can be concluded that $\partial_{\tau^*} A_{zz}^*$ leads to various $\xi \in (0.6, 1)$ for different τ_c . The corresponding A_{zz}^* is close to the case of $\xi \in (0.8, 1)$.

Then we can input the results of $A_{zz,1}$ from Fig. S8 into (S20) as initial conditions to obtain the relationship of $\lambda_{f,OB}/\lambda$ with τ_c as shown in Fig. S9. Noting that for the pre-stretch stage, as described by the VC model, $\tau_c = 6\eta_s R_0 / \gamma \lambda$, the results reveal the size effects of R_0 , as displayed in Fig. S9.

However, this analysis introduces an additional variable, ξ , that must be considered. If the experimental results are interpreted using this approximate formula, as exemplified by PEOvis in Fig. S9, the unknown parameters λ , b , and ξ must be simultaneously accounted for. Under such conditions, determining the true relaxation time λ becomes challenging.

C. Full model

By defining the dimensionless variables $\tau = t/\lambda$, $\beta = \eta_s/(\eta_p + \eta_s)$, $a = R/R_0$, $Ec = \lambda\gamma/\eta_p R_0$, and $E = \dot{\epsilon}\lambda$, the original governing equations in (S9) are transformed into their non-dimensional form as

$$\frac{Ec}{a} = \frac{3\beta}{1-\beta}E + f(A_{zz} - A_{rr}) \quad (\text{S29a})$$

$$\partial_{\tau} A_{zz} = (2E - f) A_{zz} + 1 \quad (\text{S29b})$$

$$\partial_{\tau} A_{rr} = (-E - f) A_{rr} + 1 \quad (\text{S29c})$$

$$\partial_{\tau} a = -\frac{aE}{2} \quad (\text{S29d})$$

where $f = (b-3)/(b-A_{zz}-2A_{rr})$, b is the extensibility of the polymer.

1. Analytical analysis

Considering $b \sim A_{zz} \gg A_{rr}$ yields

$$\frac{Ec}{a} = -\frac{6\beta}{1-\beta} \frac{1}{a} \frac{da}{d\tau} + \frac{bA_{zz}}{b-A_{zz}} \quad (\text{S30a})$$

$$\frac{dA_{zz}}{d\tau} = -\left(\frac{4}{a} \frac{da}{d\tau} + \frac{1}{1-A_{zz}/b}\right) A_{zz} + 1. \quad (\text{S30b})$$

Letting $A_{zz}/b = \tilde{A}$ and $Ec/b = \tilde{E}c$, this set of equations can be written as

$$\frac{6\beta}{1-\beta} \frac{1}{ab} \frac{da}{d\tau} + \frac{\tilde{E}c}{a} = \frac{\tilde{A}}{1-\tilde{A}} \quad (\text{S31a})$$

$$\frac{d\tilde{A}}{d\tau} + \frac{4\tilde{A}}{a} \frac{da}{d\tau} = -\frac{\tilde{A}}{1-\tilde{A}}, \quad (\text{S31b})$$

where $\tilde{A}(\tau=0) = 1/b$ and $a(\tau=0) = 1$. By substituting $\partial_{\tau} a/a = -1/4(1-\tilde{A}) - \partial_{\tau} \tilde{A}/4\tilde{A}$ from (S31b) into (S31a), we find

$$\frac{6\beta}{1-\beta} \frac{1}{b} \left(\frac{1}{4(1-\tilde{A})} + \frac{1}{4\tilde{A}} \frac{d\tilde{A}}{d\tau} \right) + \frac{\tilde{A}}{1-\tilde{A}} = \frac{\tilde{E}c}{a}. \quad (\text{S32})$$

When $\tau = \mathcal{O}(1)$ and $b \gg 1$, we can obtain approximately $a = \tilde{E}c(\tilde{A}^{-1} - 1)$ and substitute it into (S31b), yielding

$$\frac{d\tilde{A}}{d\tau} = \frac{\tilde{A}}{3+\tilde{A}} \Rightarrow \tilde{A}(\tau) - \tilde{A}(\tau=\epsilon) + 3 \ln \frac{\tilde{A}(\tau)}{\tilde{A}(\tau=\epsilon)} = \tau - \epsilon \quad (\text{S33})$$

where $\epsilon \sim b^{-1} \ll 1$. When considering $\tilde{\tau} = b\tau = \mathcal{O}(1)$, (S31a) and (S31b) are converted into

$$\frac{6\beta}{1-\beta} \frac{1}{a} \frac{da}{d\tilde{\tau}} + \frac{\tilde{E}c}{a} = \frac{A_{zz}}{b - A_{zz}} \quad (\text{S34a})$$

$$\frac{dA_{zz}}{d\tilde{\tau}} + \frac{4A_{zz}}{a} \frac{da}{d\tilde{\tau}} = - \underbrace{\frac{A_{zz}}{b - A_{zz}}}_{A_{zz} \ll b, b \gg 1} \approx 0 \quad (\text{S34b})$$

By substituting $A_{zz} = a^{-4}$ from (S34b) with the initial conditions of $A(0) = a(0) = 1$ into (S34a), we can obtain

$$\frac{6\beta}{1-\beta} \frac{da}{d\tilde{\tau}} = \frac{a}{a^4b - 1} - \tilde{E}c \quad (\text{S35})$$

which can be transformed and integrated along with time, yielding

$$\tilde{\tau}(a) = \int_1^a \frac{6\beta}{1-\beta} \frac{(bx^4 - 1)}{x - x^4b\tilde{E}c + \tilde{E}c} dx \quad (\text{S36})$$

This demonstrates that the full model (S29) does not yield an explicit and straightforward approximate solution.

2. Numerical results

The governing equations (S29) can be solved numerically. We solved the equations using MATLAB's `ode15s` solver, with absolute and relative tolerances set to 10^{-12} . As an example, numerical results were obtained for $b = 10^4$, $\beta = 0.95$, and $Ec \in \{10^2, 10^3, 10^4\}$, with the outcomes of dimensionless diameter $a(\tau)$, conformation A_{zz} and A_{rr} , $\lambda_e/\lambda = \log_{10}(2/3E)$ and elastic-viscous stress ratio $\xi = \sigma_p/\sigma_s$, as presented in Figs. S10(a-e). The onset of the EC phase was determined by calculating the maximum value of $2/3E$ when it is less than 1, as this corresponds to the point where the slope of the $a(\tau)$ curve is minimized. The solid markers in the figure represent the points at which λ_e/λ were determined numerically.

Subsequently, we varied the conditions across $\beta \in \{0.05 : 0.05 : 0.95\}$, $b \in \{10^2 : 10 : 10^6\}$, and $Ec \in \{10^1 : 10 : 10^5\}$ to calculate the variation of λ_e/λ . The results (Fig. S10(f)) indicate that λ_e/λ is primarily influenced by Ec and b , with negligible dependence on β when $\beta \gtrsim 0.8$. This observation allows us to construct a two-dimensional phase diagram of λ_e/λ as a function of Ec and b , as shown in Fig. S10(g), which intuitively illustrates that smaller Ec and larger b result in λ_e being closer to the true relaxation time λ . However, considering that Ec contains λ , which cannot be directly measured experimentally, we transform the phase diagram into a plot of Ec_e and b (Fig. 4 in the main text).

3. Determine actually relaxation time

Following the comparison of $\lambda_e/\lambda_{e,min}$ and λ_e/λ between experimental and numerical results, as introduced in the main text, one can obtain the actual relaxation time λ and extensibility b as shown in Fig. 3 for PEO-PEG-8M and Fig. S11 for PEOvis.

V. ESTIMATION OF FILAMENT DIAMETER D_0 IN BREAKUP FOR DRIPPING AND DOS METHOD

In the dripping and DoS methods, liquid breakup is triggered by the stretching of the liquid column due to the droplet's own weight or spreading on a solid surface. Consequently, the initial minimum diameter of the suspended droplet, defined by the nozzle outer diameter ℓ , does not correspond to the initial diameter D_0 governing the breakup dynamics. In contrast, in the stepwise-controlled stretching between two parallel plates, the initial breakup diameter D_0 can be directly observed [1]. Therefore, in this study, we determine the initial breakup diameter D_0 based on the fundamental assumption of the full model, which considers a uniform liquid column. Through image recognition processing, we extract the liquid column diameter D and approximate length L , and define the initial breakup diameter when the aspect ratio L/D satisfies $1 \lesssim L/D \lesssim 3$. Under this assumption, we examine the influence of selecting $L/D \approx 1, 2, \text{ and } 3$ on the extraction of the actual relaxation time, as shown in Fig. S12 by taking PEO-PEG-8M for example. It is observed that within this range of D_0 , the conclusions regarding λ and b remain unaffected, corroborating the robustness of our proposed criterion.

* nh0529@princeton.edu

† hastone@princeton.edu

- [1] A. Gaillard, M. A. Herrada, A. Deblais, J. Eggers, and D. Bonn, *Phys. Rev. Fluids* **9** (2024), 10.1103/physrevfluids.9.073302.
- [2] V. Calabrese, A. Q. Shen, and S. J. Haward, "Effects of polydispersity and concentration on elastocapillary thinning of dilute polymer solutions," (2024).
- [3] V. Tirtaatmadja, G. H. McKinley, and J. J. Cooper-White, *Phys. Fluids* **18** (2006), 10.1063/1.2190469.
- [4] R. M. Johnson, J. L. Schrag, and J. D. Ferry, *Polym. J.* **1**, 742 (1970).
- [5] M. Rubinstein and R. H. Colby, *Polymer physics* (Oxford university press, 2003).
- [6] M. Alves, P. Oliveira, and F. Pinho, *Annu. Rev. Fluid Mech.* **53**, 509–541 (2021).
- [7] V. Entov and E. Hinch, *J. Non-Newtonian Fluid Mech.* **72**, 31–53 (1997).
- [8] C. Wagner, L. Bourouiba, and G. H. McKinley, *J. Non-Newtonian Fluid Mech.* **218**, 53–61 (2015).

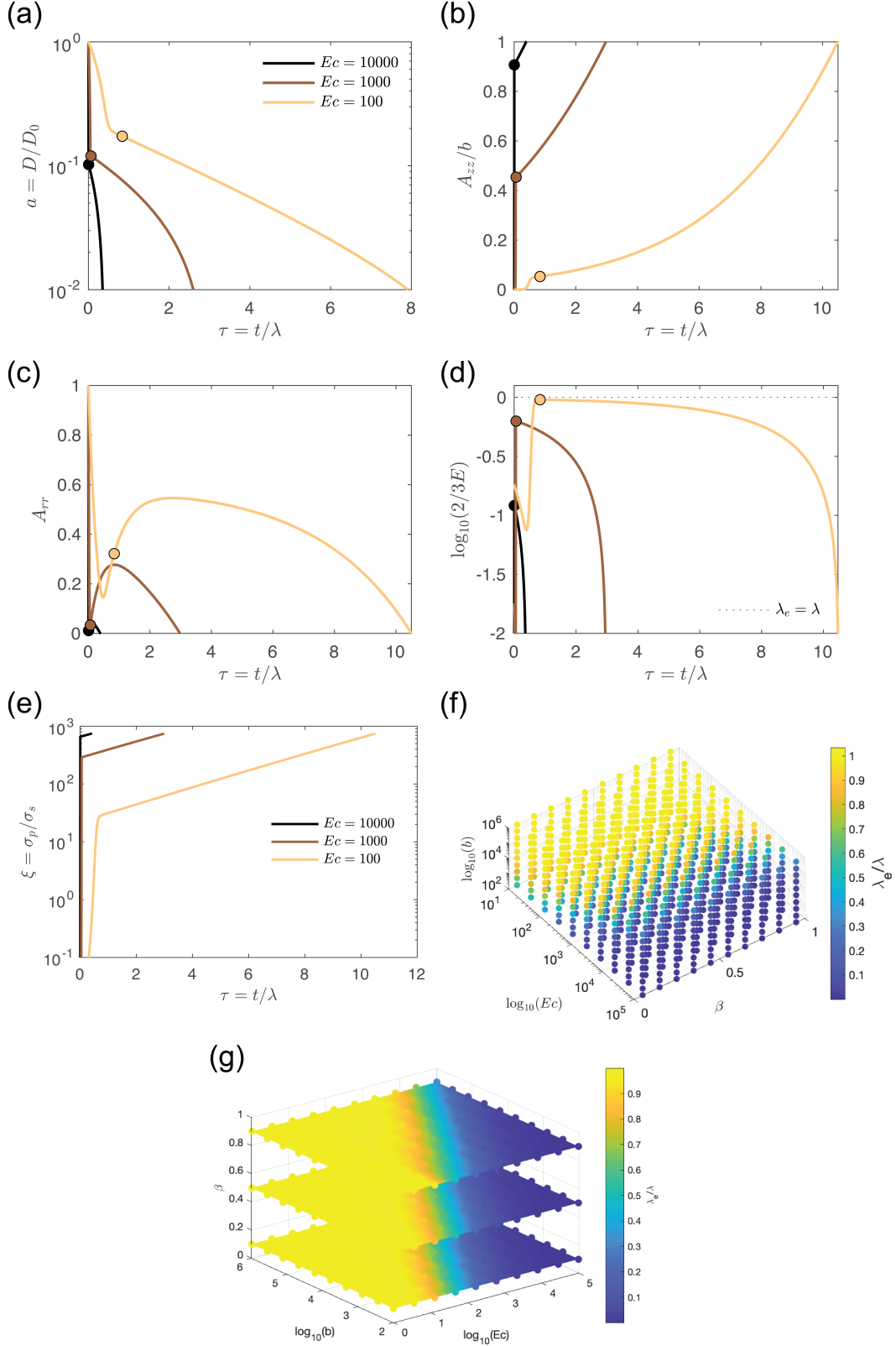


Fig. S10. Numerical results of the full model. Variations of (a) dimensionless diameter a , (b) normalized conformation component A_{zz}/b and (c) conformation component A_{rr} , and $2/3E$ versus dimensionless time τ , under the conditions of $\beta = 0.95$, $b = 10^4$ and $Ec = 2\gamma\lambda/(D_0\eta_p) \in \{10^2, 10^3, 10^4\}$. The solid symbols represent the point we can obtain the $\lambda_e/\lambda = 2/3E$ from the slope of $a(\tau)$ based on the numerical results. (e) Evolution of elastic-viscous stress ratio $\xi = \sigma_p/\sigma_s$ during breakup for $Ec \in \{10^2, 10^3, 10^4\}$ (f) Comparison of λ_e/λ under the varying conditions of $\beta \in \{0.05 : 0.05 : 0.95\}$, $b \in \{10^2 : 10 : 10^6\}$ and $Ec \in \{10^1 : 10 : 10^5\}$. (g) Phase map of λ_e/λ along with b and Ec at specific $\beta \in \{0.1, 0.5, 0.9\}$.

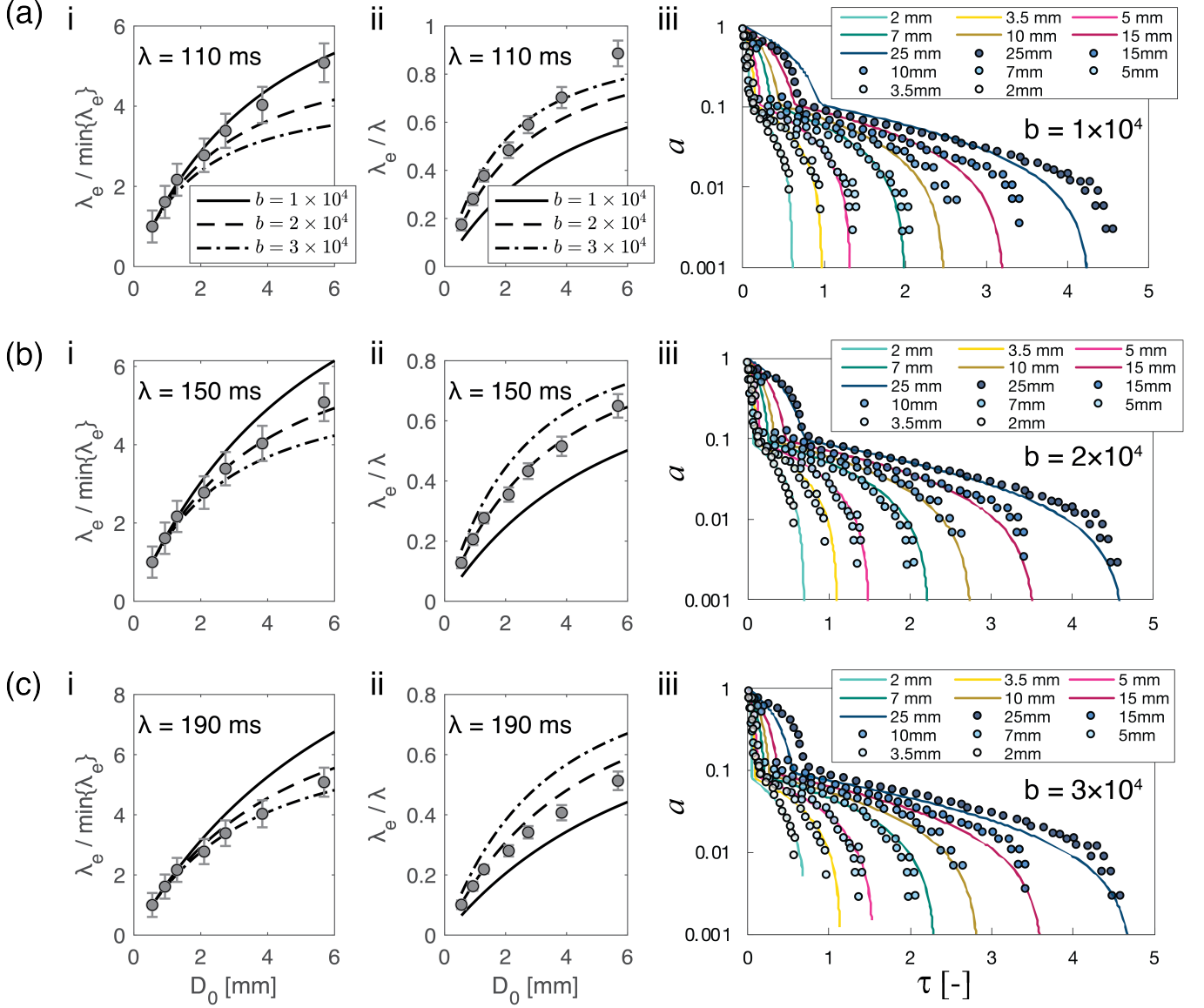


Fig. S11. Predicted results based on the procedure in Section IV-C3 using $\lambda = 110$ ms (a-i,ii), $\lambda = 150$ ms (b-i,ii), and $\lambda = 190$ ms (c-i,ii). Panels (a-iii, b-iii, c-iii) show the corresponding comparisons with $a(\tau)$ for the dataset from Ref. [1]. The results suggest that $(\lambda, b) = (150 \text{ ms}, 2 \times 10^4)$ provides a better estimate compared to $(\lambda_{e,\max} = 110 \text{ ms}, b = 2 \times 10^4)$, as proposed in Ref. [1], which was based on the maximum measured $\lambda_{e,\max}$.

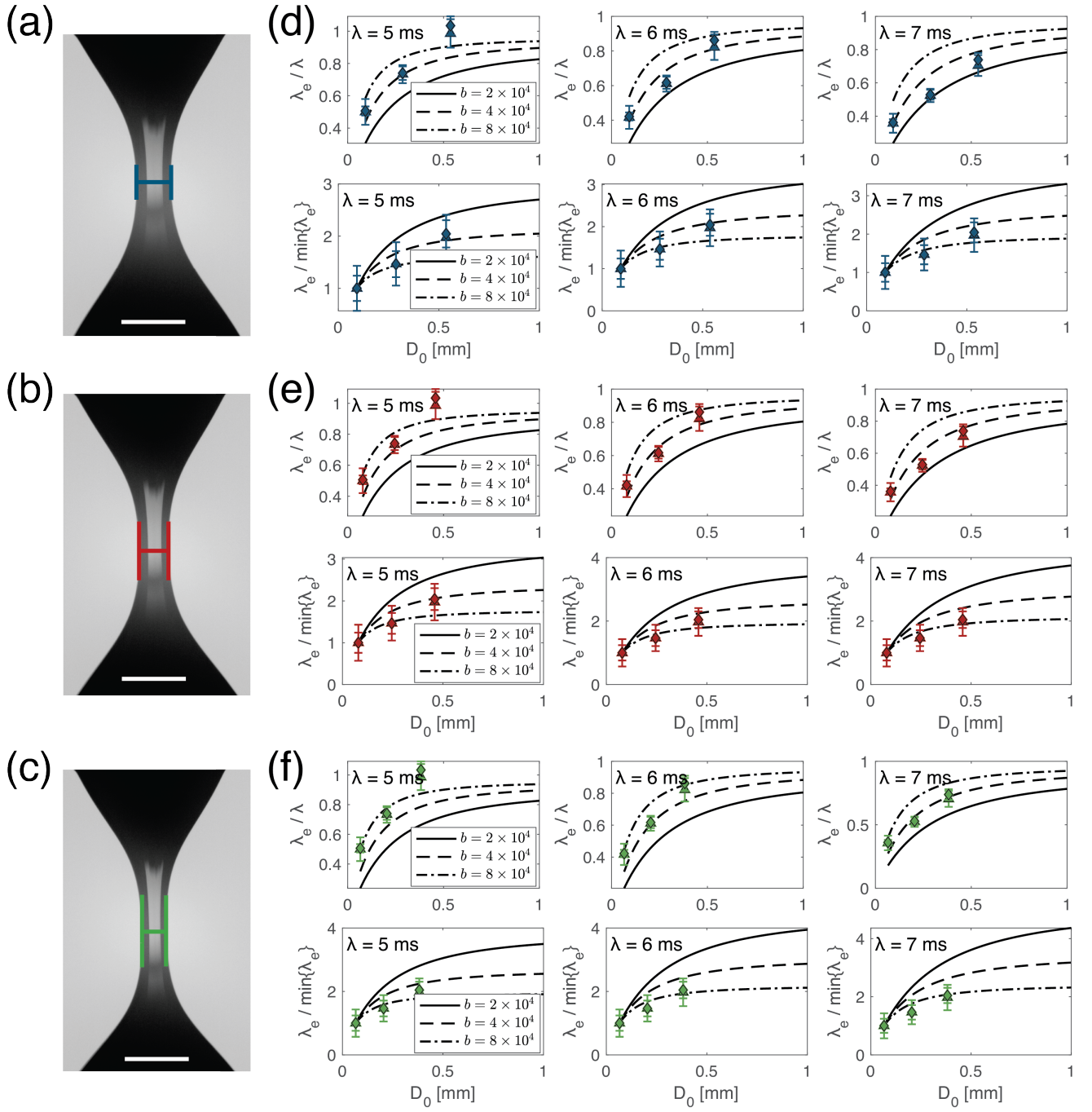


Fig. S12. Comparison of different choices of D_0 in extracting the actual relaxation time λ . Based on conditions determined from aspect ratios $L/D \approx$ (a) 1, (b) 2, and (c) 3, we evaluate $\lambda_e/\lambda_{e,\min}$ and λ_e/λ following the same procedure. The corresponding results, shown in (d-f), indicate that selecting the aspect ratio within $1 \lesssim L/D \lesssim 3$ provides a reliable criterion. The white scale bar in (a-c) represents 1 mm.